OE Optical Engineering

RESEARCH PAPER

Design and validation of a dual-wavelength, dual-beam digital holography wavefront sensor

James Mitchell* **and Stanislav Gordeyev**

University of Notre Dame, Aerospace and Mechanical Engineering Department, Notre Dame, Indiana, United States

ABSTRACT. The design and validation of a dual-wavelength and dual-beam digital holography wavefront sensor for quantitative simultaneous measurements of aero-optical wavefronts in subsonic compressible flow over two apertures are presented. The optical setup and processing methodology for reconstructing independently measured optical path difference (OPD) fields from interference patterns generated by two laser beams separated spatially along the streamwise axis are described in detail. The agreement and accuracy of the reconstructed wavefronts in a turbulent boundary layer flow are assessed, and the error among the OPD fields reconstructed from each beam is quantified using a normalized L_2-norm relative error metric. In addition, both a two-dimensional Fourier transform-based dispersion analysis and cross-correlation analysis were performed, with dispersion analysis used to estimate the convective speed of aero-optical distortions in the boundary-layer-dominated flow. We demonstrate consistent agreement between the two OPD fields, with errors being largely independent of flow speed and convective speeds matching expected values. A synthetic wavelength wavefront constructed from the complex optical fields of the two beams successfully reproduces the large-scale wavefront structure, consistent with the expected synthetic reconstruction behavior. These results validate dual-wavelength, dual-beam digital holography as a reliable method of high-resolution wavefront sensing in compressible flow environments.

© 2026 Society of Photo-Optical Instrumentation Engineers (SPIE) [DOI: 10.1117/1.OE.65.5.055106]

Keywords: aero-optics; boundary layer; digital holography; optical path difference; wavefront sensing

Paper 20250938G received Nov. 5, 2025; revised Apr. 18, 2026; accepted Apr. 20, 2026; published May 14, 2026.

1 Introduction

When light travels through a flow field with varying spatial density, the light beam becomes distorted, as the index of refraction, n, is proportional to the density

$$n(x, y, z, t) = 1 + K_{\mathrm{GD}}(\lambda)\rho(x, y, z, t), \tag{1}$$

where $K_{\mathrm{GD}}(\lambda)$ is the Gladstone–Dale constant. Although the value of K_{GD} is generally a function of wavelength λ,[1] its variation across the visible spectrum is small. The resulting aero-optical distortions, denoted by the optical path difference (OPD), are proportional to the integral of the fluctuating density field

$$\mathrm{OPD}(x, y, t) = K_{\mathrm{GD}} \int \rho'(x, y, z, t) dz, \tag{2}$$

*Address all correspondence to James Mitchell, jmitch24@nd.edu

0091-3286/2026/$28.00 © 2026 SPIE

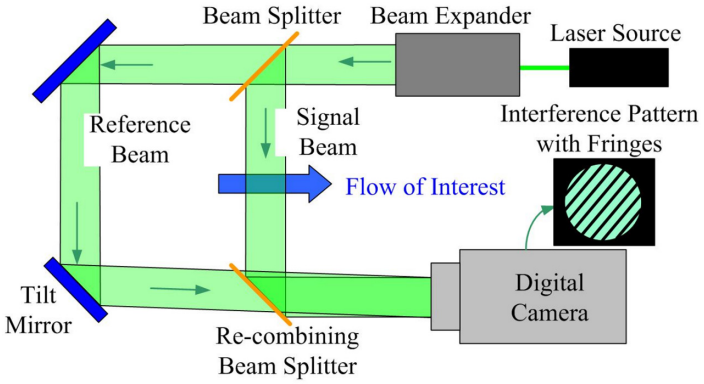


Fig. 1 Schematic of the digital holography wavefront sensor. The signal beam, distorted by a flow of interest, is combined with the reference beam from the same coherent laser source. A small angular offset among them creates an interferometric fringe pattern. The resulting fringe pattern is recorded by a camera.

where the integration is performed in the propagation direction of the beam.[2,3] These optical distortions can significantly affect the propagation of the beam, leading to loss of beam intensity and deterioration (blurring) of visual representations of objects.[2,4] Therefore, careful measurements and analysis of the wavefronts, distorted by turbulent flows, are essential to study the sources of aero-optical distortions and various means to mitigate them. Two of the most common wavefront sensors to measure spatio-temporally resolved wavefronts are the Shack–Hartmann wavefront sensor (SHWFS) and the digital holographic wavefront sensor (DHWFS). Although the concept of digital holography was proposed shortly after the invention of lasers,[5] DHWFS became popular with the advancements in digital cameras in the late 1990s.[6–8] In aerospace research, DHWFS as a sensor to measure fast-changing aero-optical distortions was introduced relatively recently[9,10] and is rapidly gaining popularity due to better spatial resolution compared with SHWFS, as well as better performance in the presence of shock-related wavefront gradients.[11]

The principle of operation of the digital holography sensor is presented in Fig. 1. The laser beam, either pulsed or continuous, with a sufficiently large coherence length, is expanded and collimated using a beam expander and split into two beams: a signal beam and a reference beam. The signal beam propagates through a flow of interest and collects wavefront distortions along its path. It is then recombined with the reference beam from the same laser source to form an interference pattern. The interference pattern is recorded using a digital camera with an adequate spatial resolution. The tilt mirror is used to introduce a small angle between the signal and the reference beams before combining them on the digital camera, resulting in a fringe pattern in the image. The technique works for a single image; however, a high-speed digital camera is often used to properly capture the temporal evolution of unsteady interference images and underlying optical distortions.

The total intensity of the fringe pattern, I, is the superposition of the complex optical fields of the signal and reference beams, U_S and U_R, respectively

$$I = |U_S + U_R|^2 = |U_S|^2 + |U_R|^2 + U_S U_R^* + U_S^* U_R, \tag{3}$$

where the asterisk denotes complex conjugate. The terms $|U_S|^2$ and $|U_R|^2$ are the real-only terms, which are ignored as they do not contribute to the phase information imposed on the signal beam.[12] An example of the interference pattern is shown in Fig. 2(a). Both $U_S U_R^*$ and $U_S^* U_R$ contain wavefront distortion information, but since $U_S U_R^*$ and $U_S^* U_R$ are complex conjugates of each other, only one term is needed to find the distorted optical complex field. To isolate the $U_S U_R^*$ term from the other terms, a two-dimensional spatial Fourier transform of the hologram image is performed. The result is presented in Fig. 2(b). The position of $U_S U_R^*$ in the Fourier space depends on the relative fringe spacing in the image, which depends on the angle between the signal and the reference beams on the image plane, and it can be shifted in the Fourier space by moving the tilt mirror and separating this term from the contaminating effects of the central

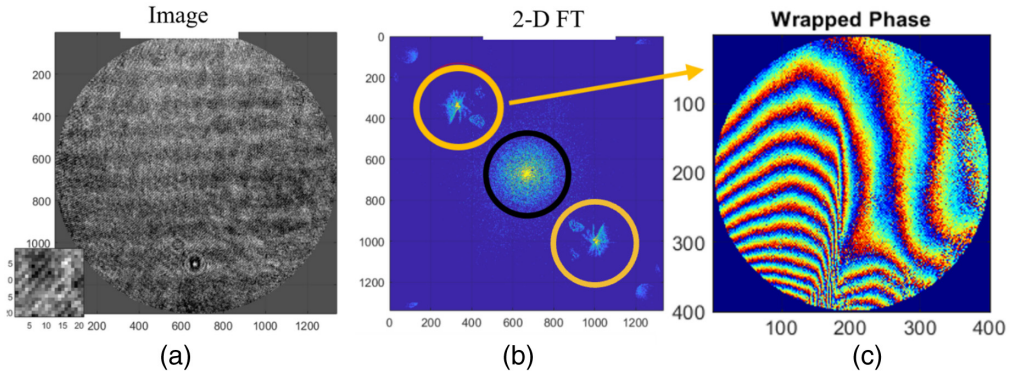


Fig. 2 (a) Holographic image, with a cutout showing the details of the finely spaced fringes. (b) Image's 2D Fourier transform. The orange circles correspond to the information-carrying $U_S U_R^*$ and $U_S^* U_R$ terms, and the black circle corresponds to the central $|U_S|^2 + |U_R|^2$ term. After selecting the signal-related peak, indicated by either of the orange circles, the inverse 2D Fourier transform is performed to recover the wrapped phase, shown in panel (c).

(real-only) term in the Fourier space. All unwanted terms (i.e., $U_S^* U_R$, $|U_S|^2$, and $|U_R|^2$) are filtered out by selecting only the off-axis peak circled in orange in Fig. 2(b). After isolating $U_S U_R^*$, the inverse Fourier transform is performed to recover both the amplitude and the phase of the distorted wavefront field. The resulting phase field is shown in Fig. 2(c).

By definition, the phase is wrapped between $-\pi$ and π and must be unwrapped before it can be related to a wavefront. There are several algorithms for unwrapping the phase,[13,14] but in general, they cannot correctly unwrap the phase map when there are sharp wavefront gradients. For sufficiently large phase changes, the phase differences between two adjacent pixels become larger than π, leading to a non-unique reconstruction of the phase field. To address this problem, a dual-wavelength digital holography (DH) sensor is proposed.[15–20] For dual-wavelength DH sensors, two co-aligned beams with different wavelengths, λ_1 and λ_2, are propagated through the flow of interest, and two complex optical fields at these wavelengths, $U_{S,1}$ and $U_{S,2}$, are simultaneously measured. A phase can be computed from complex optical fields of each beam as[16,17]

$$\Phi_{\text{syn}} = \arg(U_{S,1} U_{S,2}^*). \tag{4}$$

This phase map corresponds to a new "synthetic" phase map, which corresponds to a much longer "synthetic" wavelength than that of either individual beam. The synthetic wavelength is given by

$$\lambda_{\text{syn}} = \frac{\lambda_1 \lambda_2}{|\lambda_1 - \lambda_2|}. \tag{5}$$

With a proper choice of λ_1 and λ_2, the resulting synthetic wavelength phase field remains within $[-\pi, \pi]$, eliminating the need for phase unwrapping entirely. In practice, however, these choices of λ_1 and λ_2 often depend on available lasers, and the synthetic wavelength instead reduces the spatial density of phase wraps rather than eliminating them entirely.

In addition to its dual-wavelength capability, the sensor can also operate in a dual-beam configuration. Because both wavefronts are recorded simultaneously on the same digital sensor, the system can perform simultaneous measurements at different spatial locations within the flow. This is achieved by optically separating the signal beams and directing them through distinct regions of the flow before recombining them with their corresponding reference beams at the camera. By imposing different reference beam tilts, the resulting $U_S U_R^*$ and $U_S^* U_R$ terms are separated in the Fourier domain and individually isolated using the filtering procedure described previously.

In the present validation study, the studied flow exhibits sufficiently low phase gradients that phase unwrapping can be performed reliably at each wavelength independently, and the synthetic wavelength is not required for reconstruction. The synthetic wavelength formulation is nevertheless implemented and briefly evaluated to verify its expected behavior. However, the primary objective of this work is to validate the accuracy and robustness of the individual single-wavelength measurements. Therefore, the two wavelengths are treated independently throughout most of the

analysis. Establishing this agreement ensures that the synthetic phase map can be constructed with confidence when the sensor is applied to flows with stronger phase gradients, where the synthetic wavelength becomes essential.

In this work, we present a dual-wavelength, dual-beam digital holography wavefront sensor capable of simultaneously reconstructing aero-optical wavefronts over two apertures, both fully overlapped and separated, using two optical wavelengths. In the case of the fully overlapped beams, the present system enables a direct internal consistency validation by comparing independently reconstructed wavefronts that represent the same physical optical distortion. The accuracy of the reconstruction is assessed through statistical agreement between the two wavelength channels, comparison with established boundary layer aero-optical scaling behavior, and measurement of convective velocities using dispersion analysis. This validation establishes the reliability of dual-wavelength digital holography measurements and provides a foundation for future application of the synthetic-wavelength formulation to flows with strong density gradients where conventional phase unwrapping fails.

2 Experimental Setup

All measurements were performed in the Trisonic Wind Tunnel (TWT) at Hessert Laboratory for Aerospace Research at the University of Notre Dame. A schematic of the TWT facility can be seen in Fig. 3. The TWT is a continuous flow indraft wind tunnel with an inlet contraction ratio of 150:1. The test section is constructed of aluminum, with a cross-section of 10 cm × 9.9 cm and a length of 130 cm from the end of the inlet to the diffuser. Optical access windows are installed on the walls of the test section from 100 to 120 cm. The freestream velocity was measured using a Pitot probe just upstream of the optical window. The aero-optical flow of interest was a boundary layer formed over the tunnel walls, and the development length of the boundary layer from the end of the inlet to the measurement location is $L = 148$ cm.

Using Pitot probe measurements of static and total pressure at the beginning of the test section, we determined the boundary layer velocity profile, from which we found our boundary layer thickness, δ, to be $\delta = 18.5 \pm 1.5$ mm.

A schematic and a labeled picture of the dual-wavelength DH sensor are shown in Figs. 4 and 5, respectively. The lasers chosen for this optical setup were the Cobolt 05-01 Series with 532-nm light and the Cobolt 05-01 Series with 640-nm light. Both lasers have a coherence length greater than 100 m, which is sufficient for current experiments. At these wavelengths, the Gladstone–Dale constants differ only by ~0.6%. Thus, for the wavelengths used in this study, K_{GD} is treated as a constant. For this experiment, the wavelengths were selected on the basis of their ability to be cleanly separated by dichroic mirrors. At the beginning of the optical path, both beams, each 0.7 mm in diameter, are guided using two steering mirrors into spatial filters comprising a microscopic objective and a 10-μm pinhole, resulting in an Airy pattern in the far field. An iris along each path clips out the Airy rings, and $f = 250$-mm lenses collimate each beam to 25 mm in diameter. Each expanded beam then passes through its own 38-mm beam cube with a 50/50 transmission/reflection ratio, separating the signal and reference beams of each wavelength. The two signal beams are then sent through a 50-mm dichroic mirror (DMLP567L, Thorlabs, Newton, New Jersey, United States) that transmits the 640-nm beam and reflects the 532-nm beam. This filter is placed along a rail to allow the beams to fully overlap or be separated

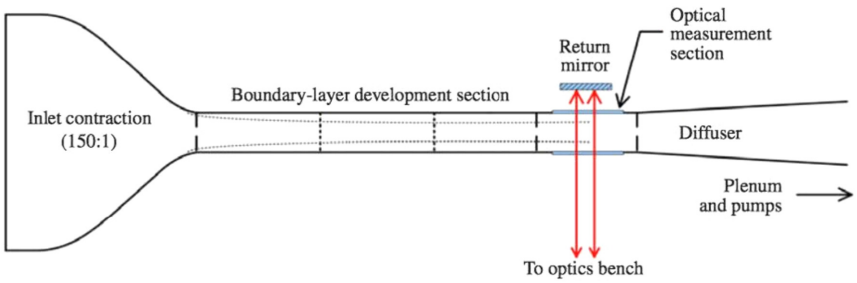


Fig. 3 Schematic of TWT facility outlining the location of the measurement section, orientation of the beams, and the location of the return mirror.

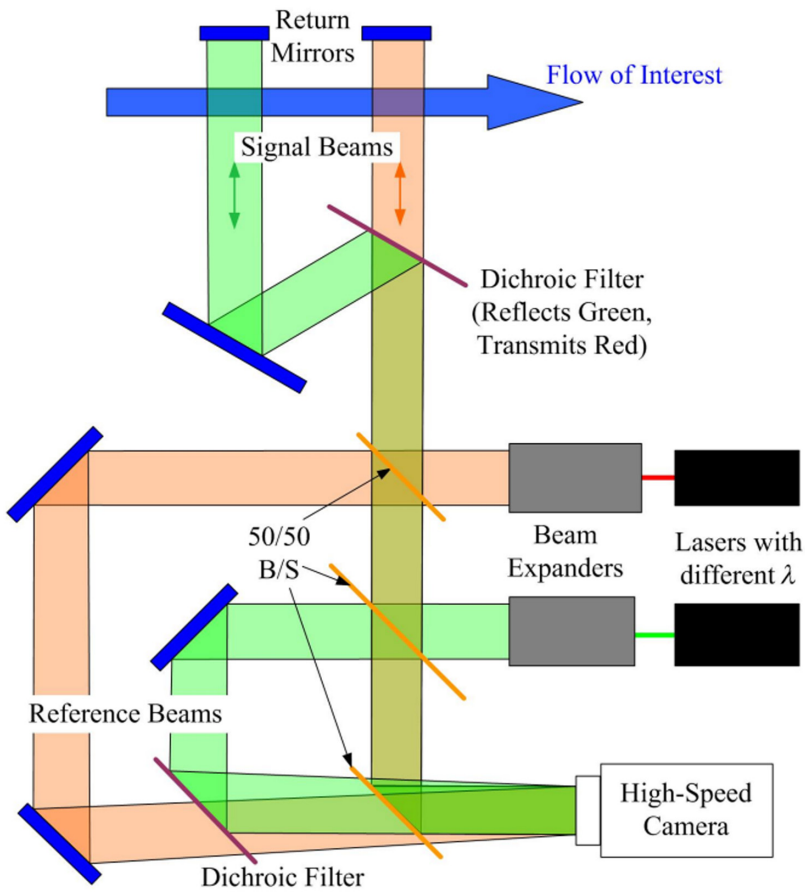


Fig. 4 Schematic of dual-wavelength DH sensor for the case of fully separated signal beams.

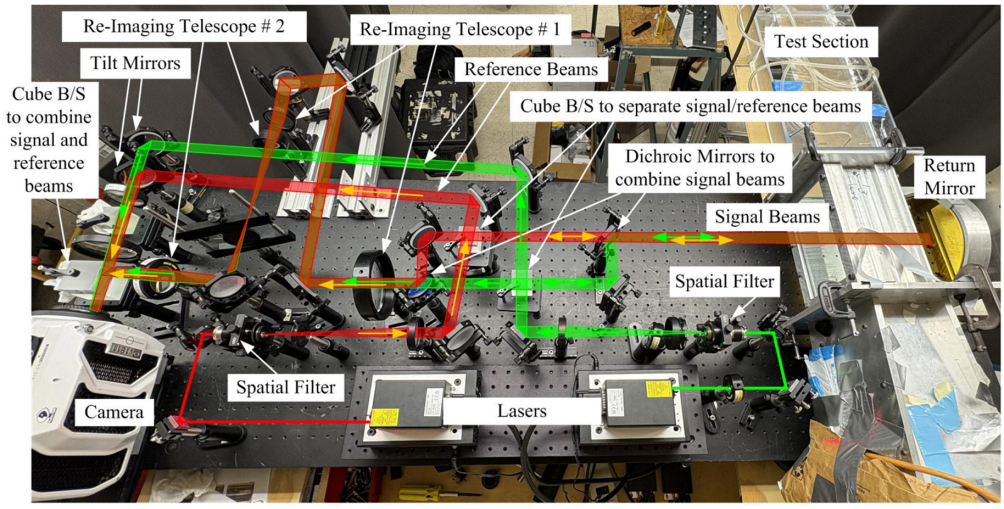


Fig. 5 Labeled picture of the digital holography sensor for the case of fully overlapped signal beams.

by a variable distance at the tunnel window. The setup in Fig. 5 shows the case when both beams were fully overlapped to perform simultaneous measurements of the same flow region. A large return mirror is placed on the far side of the tunnel, and the signal beams are returned along the same paths until they pass through the same 50/50 beam cubes mentioned previously. The reflected light that passes through the beam cubes is unused, whereas the transmitted light is recombined using a different dichroic mirror (DMSP567L, Thorlabs, Newton, New Jersey,

United States) which, unlike the first dichroic mirror, reflects the 640-nm beam and transmits the 532-nm beam. The combined signal beams are re-imaged using two consecutive $4f$ relay systems: the first composed of lenses with focal lengths of 400 and 350 mm and the second with focal lengths of 175 and 200 mm. These focal lengths are specific to the distance to the tunnel in our setup, and they re-image the image plane of the return mirror to the camera plane while having the property of 1× magnification, outputting a 25-mm beam. In one of the focal planes of the re-imaging lenses, an iris is placed to clip out any unwanted ghost beams. After the re-imaging telescopes, the combined signal beams are reflected by a 50 mm 50/50 beam cube onto the digital sensor. This beam cube is placed very close to the digital sensor to impart a variable tip and tilt on each of the signal beams without imparting a large translational displacement that would move the signal beams off of the digital sensor.

Each of the reference beams, as they are separated from their respective signal beams by the cube beam splitters, is reflected by a series of mirrors and recombined using a 50/50 beam splitter. The 532-nm beam path has two mirrors prior to transmission through the beam splitter, whereas the 640-nm beam path has a single mirror and uses the beam splitter as the other beam control component. These components are used to add tip and tilt to the reference beams while ensuring overlap with the signal beams on the camera. The 50/50 beam cube also serves as a beam intensity filter, so that the signal and reference beams are close to equal in intensity on the digital sensor. This results in the strongest interference pattern and the highest signal-to-noise ratio. To maximize the strength of the interference pattern, neutral density (ND) filters may be placed along any appropriate part of the optical path. In our setup, small intensity reductions of the red signal beam by the dichroic mirrors required the placement of a weak ND filter along a part of the optical path where the green signal beam was isolated (not labeled in Fig. 5).

The partially overlapping reference beams are then expanded by a factor of 1.5 using $f = -200$ and $f = 300$ mm lenses (not labeled in Fig. 5 to avoid clutter) to facilitate the introduction of significant tip and tilt in the reference beams while maintaining full overlap between the signal and reference beams on the digital sensor. The reference beam then passes through the final 50-mm beam cube, combining the signal and reference beams and fully overlapping them on the high-speed camera.

The resulting interference pattern was captured using a Phantom v2512 high-speed camera with a pixel width of 28 μm, a resolution of 768×768 pixels, and a sampling rate of 39 kHz.

Static and total pressure measurements were taken by a Pitot probe, installed in the middle of the measurement section, and used to find the freestream Mach number, using the isentropic relation

$$\frac{p}{p_t} = \left(1 + \frac{\gamma - 1}{2} M^2\right)^{-\frac{\gamma}{\gamma - 1}}. \tag{6}$$

The freestream velocity, $U_\infty = M \cdot a$, was calculated using the adiabatic relation for the local speed of sound, a

$$a = \sqrt{\frac{\gamma R T_0}{1 + \frac{\gamma - 1}{2} M^2}}, \tag{7}$$

where $\gamma = 1.4$ is the specific heat ratio of air, $R = 287$ J/(kg · K) is the specific gas constant for air, and $T_0 = 297$ K is the stagnation temperature of the flow.

The aero-optical measurements were acquired at three different separations between the green and red beam paths: 0 mm (a fully overlapping case); 40 mm, which is equivalent to twice the boundary layer thickness δ; and 60 mm (3δ). For each separation case, data were collected at five different Mach numbers of 0.52, 0.59, 0.65, 0.70, and 0.73. For the non-overlapping cases, the green beam was placed upstream of the red beam. A total of 4300 frames of data were taken for each case. The laser power levels were set to 600 mW, and the frame exposure time was 3 μs.

3 Data Reduction and Analysis

The process of reconstructing the corresponding wavefronts from the digital holographic image for each wavelength is as follows. The first step is to subtract the mean pixel value of the image to

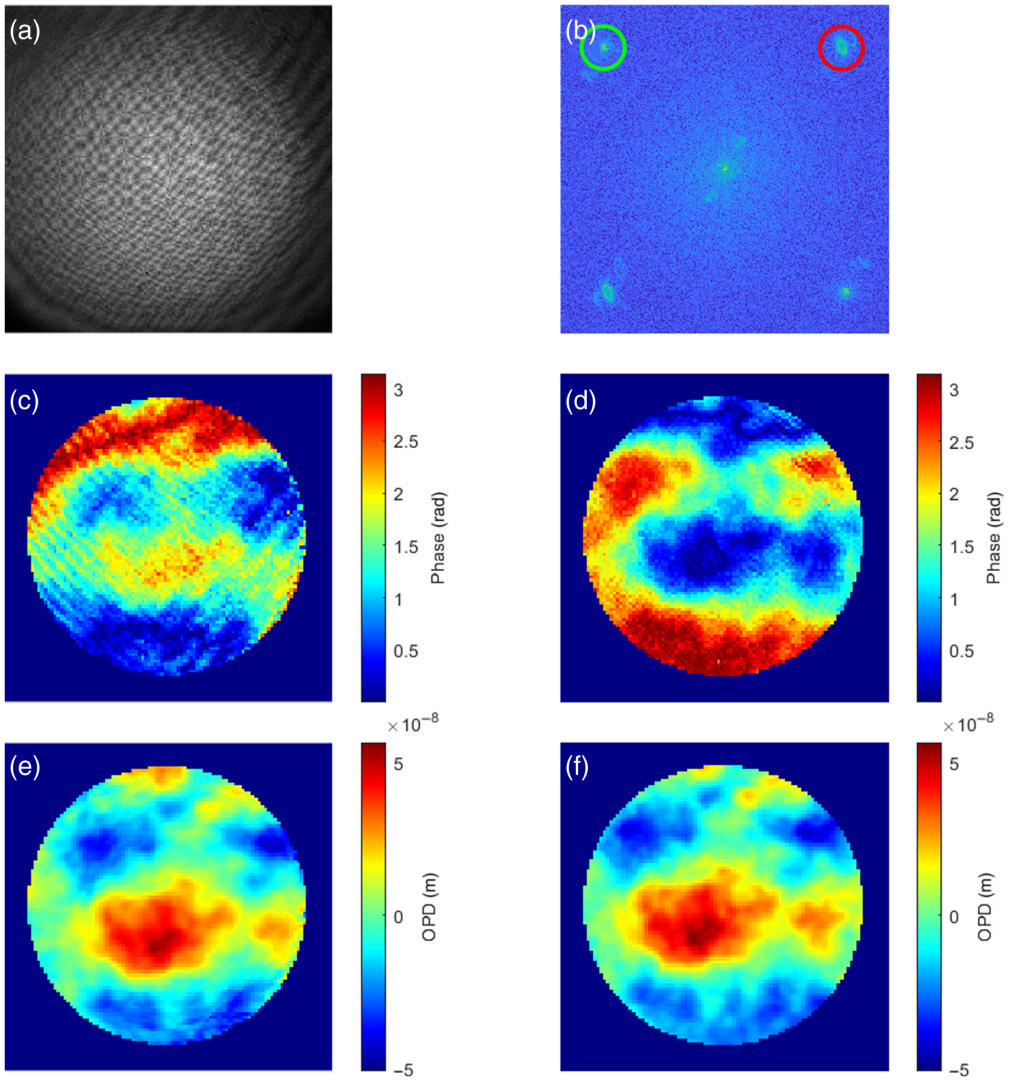


Fig. 6 Typical wavefront reconstruction for dual-wavelength digital holography. (a) Raw holographic image after DC offset removal and cropping. (b) Fourier plane showing the cross-correlation peaks for each laser beam wavelength. (c) Red beam wrapped phase field obtained after inverse Fourier transform and masking. (d) Green beam wrapped phase field obtained after inverse Fourier transform and masking. (e) Red beam final wavefront after least-squares unwrapping, tip/tilt removal, time-averaged wavefront subtraction, and ghost beam suppression. (f) Green beam final wavefront after least-squares unwrapping, tip/tilt removal, time-averaged wavefront subtraction, and ghost beam suppression.

remove the direct current (DC) offset in the Fourier plane. Then, the image is cropped tightly so that the overlapping region is centered within a square aperture to reduce the number of pixels to be analyzed and improve the signal-to-noise ratio in the Fourier plane. A representative example is shown in Fig. 6(a). Then, the MATLAB function $fft2$ is used to take a spatial two-dimensional fast Fourier transform (FFT) of the cropped image. In the Fourier plane, shown in Fig. 6(b), there is a strong central zero-order peak and two weaker cross-correlation peaks for each wavelength. As for a given beam, the two off-center peaks are complex conjugates of one another, as indicated in Eq. (3), they carry the same information, and only one is needed for reconstructing the wavefront. Each cross-correlation peak, related to either the green or the red laser beam and circled in Fig. 6(b), is then centered within a circular aperture for each of the beams. The spatial resolution of the reconstructed wavefront is equal to the pixel-wise dimensions of this circular crop, but an increased radius also will include more noise from the zero-order peak, leading to a smaller signal-to-noise ratio. The crop was implemented with a Gaussian filtering

function with a standard deviation of 16 pixels. This size of the Gaussian filter was selected after some trial-and-error to minimize spectral leakage from the zero-order peak and contamination from ghost beams while remaining sufficiently large to capture the dominant spatial frequencies of the reconstructed wavefront.

After the crop, an inverse two-dimensional Fourier transform is performed on each circular aperture using the MATLAB function $ifft2$, resulting in 2π-wrapped phase maps, shown in Figs. 6(c) and 6(d) for the red beam and the green beam, respectively. At this point, no-flow subtraction occurs. Prior to processing flow cases, the no-flow case is fully processed so that, at this stage, the time-averaged unwrapped no-flow complex optical field can be subtracted from the flow case. A circular mask is then applied to the wrapped phases to mask any noise surrounding the circular overlap region, greatly improving unwrapping performance. All pixels outside the chosen circular aperture are converted to Not-a-Number (NaN) values.

To recover OPD from the wrapped phase, we performed phase unwrapping using the least-squares method, which minimizes the sum of the squared differences between the gradient of the unwrapped phase solution and that of the measured wrapped phase.

At this point, the tip/tilt and piston are calculated for the reconstructed wavefront using a least-squares plane fit and then subtracted from the wavefront. The resulting wavefronts are plotted in Figs. 6(e) and 6(f) for the red and the green beams, respectively. As expected for the fully overlapping beam case, the wavefronts in these subplots exhibit the same dominant large-scale spatial structures. Additional analysis of the differences between the wavefronts from the red and the green beams will be presented in Sec. 4.1.

Ghost beams caused by back-reflections in beam cubes or other optical components may appear in the Fourier plane in Fig. 6(b). The circular Fourier aperture should also be used to crop out these ghosts as best as possible to avoid nonphysical contributions to the reconstructed OPD. Ghost beams that could not be eliminated using a crop in the Fourier plane create fringes in the OPD field. An example of this is shown in Fig. 7(a). To eliminate these additional ghost beams, a second spatial two-dimensional fast Fourier transform was taken of the data [see Fig. 7(b)], and local masks were applied in Fourier space at the peaks corresponding to those fringes to suppress those frequencies. The masks were implemented as Gaussian attenuation functions that smoothly reduce the spectral amplitude near each peak. An inverse FFT was then performed to return the data to the spatial domain, with the final result plotted in Fig. 7(c).

For each instantaneous frame, a moving mean over 101 frames centered on that frame was subtracted to remove slowly varying or stationary components of the wavefront due to steady lensing effects. This window length was selected to be significantly longer than the wavefront decorrelation time, ensuring that turbulent fluctuations average to zero while preserving only the stationary component. The resulting signal therefore represents only the unsteady portion of the OPD. Finally, all resulting OPD data were divided by $2\sqrt{2}$ to account for the double-pass setup and the presence of two boundary layers on both tunnel walls.[2]

A small number of frames were excluded from the analysis due to corruption, identified by an abnormally high fraction of zero-valued pixels. These frames were automatically flagged and replaced with NaN values prior to post-processing.

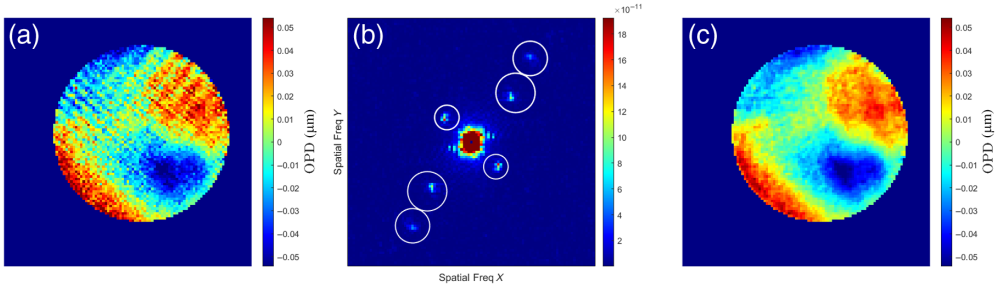


Fig. 7 Fringe removal due to the presence of ghost beams using the Fourier masking. (a) OPD before the Fourier masking. (b) 2D Fourier transform of the wavefront, with circles around the ghost beam regions to be masked. (c) Reconstructed OPD after masking out the ghost beams and performing the inverse 2D Fourier transform.

4 Results

4.1 Fully Overlapping Case

Even when the beams looked perfectly overlapped, a small lateral offset was observed among the beams, mainly in the horizontal direction. This small spatial shift can be seen in Figs. 6(e) and 6(f). For each fully overlapping case, this integer offset was found and removed by minimizing the root mean square of the OPD field given by the difference between the green beam- and red beam-measured OPDs to better align the beams. This difference among the wavefronts will be referred to in this paper as a differential OPD field. After shifting one field to overlap with the other, only pixels shared among the original OPD fields were kept for analysis. The present low-gradient case serves as a controlled validation environment in which the two wavelengths should reconstruct identical physical wavefronts, allowing for the direct assessment of reconstruction consistency.

Figure 8 presents a side-by-side comparison of the OPD fields reconstructed from the red and green beams, together with the resulting differential OPD field. The same turbulent flow structures are clearly evident both in Figs. 8(a) and 8(b), demonstrating that dual-wavelength DH can reliably measure the same optical field with two beams of different wavelengths.

Importantly, the absence of coherent structures in the differential OPD indicates that there are no significant systematic discrepancies between the two reconstructions, reinforcing the agreement between the red and green reconstructed OPD fields.

We calculated the time-averaged spatial variation of the OPD fields for the green, red, and synthetic beams for each flow speed, defined as

$$\mathrm{OPD}_{\mathrm{rms}} = \sqrt{\overline{\langle [\mathrm{OPD}(x,y,t)]^2 \rangle_{x,y}}}. \tag{8}$$

To quantify the relative error between wavefronts measured by two beams for the fully overlapped case, a relative error in the L_2-norm, $\Sigma(t)$, was computed for each frame and for all Mach numbers, where $\Sigma(t)$ is given by

$$\Sigma(t) = \sqrt{\frac{\langle [\mathrm{OPD}_1(x,y,t) - \mathrm{OPD}_2(x,y,t)]^2 \rangle_{x,y}}{\mathrm{OPD}_{\mathrm{rms},1}\mathrm{OPD}_{\mathrm{rms},2}}}, \tag{9}$$

where the angular brackets indicate the spatial averaging over the aperture, and sub-indices "1" and "2" denote the red and the green beams, respectively. The quantity $\Sigma(t)$ represents the relative root mean square deviation between the two wavefronts. In addition, the time-averaged value of the relative error, $\Sigma = \overline{\Sigma(t)}$, and the standard deviation, $\sigma_\Sigma = \overline{[(\Sigma(t) - \Sigma)^2]}^{1/2}$, were also computed. Σ and σ_Σ values for the fully overlapped case are presented in Table 1. The normalized errors are ~20%, with the standard deviations of 4% to 6%, with the error generally going down with the increasing speed.

To further investigate the discrepancies among the beams, we computed the probability density function of the normalized relative error, $\Sigma(t)$, calculated using Eq. (9), for each frame. This distribution is presented in Fig. 9 for the $M = 0.70$ case and characterizes the frame-to-frame variability of the spatial error. The probability distribution is highly asymmetric with a long tail,

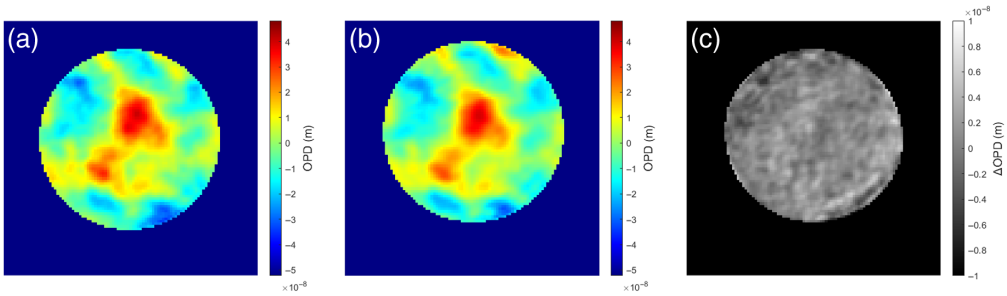


Fig. 8 Reconstructed OPD fields for the fully overlapping case. (a) OPD measured with the green (532 nm) beam. (b) OPD measured with the red (640 nm) beam after shifting by the pixel offset. (c) Difference between the two fields after alignment. Note that the range of color values was reduced, compared with panels (a) and (b), to better demonstrate the difference among the wavefronts.

Table 1 Mean and standard deviations of normalized errors for the fully overlapped beams at each flow speed.

Mach number	Σ (%)	σ_Σ (%)
0.52	21.1	4.40
0.59	19.6	5.00
0.65	18.7	5.74
0.70	17.9	4.58
0.73	17.6	5.45

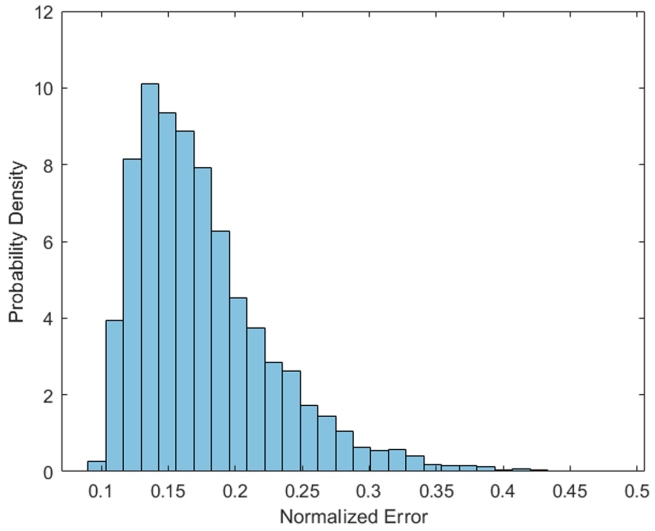


Fig. 9 Probability density function of the normalized error, Eq. (9), between two fully overlapped beams for the $M = 0.70$ case.

resembling a log-normal distribution, which is typical for non-negative error distributions. It indicates that most of the time, wavefronts computed from the red and green beams are similar, within 20%, to each other. Only a small percentage of the wavefronts exhibit large discrepancies, up to 40%. The inspection of individual wavefronts showed that the main reason for the discrepancy is the presence of fine-scale noise in the red beam wavefronts, observed in the difference plot in Fig. 8(c). One possible reason for this noise is that the Gaussian filter, applied to isolate the signal peaks, potentially removes different amounts of small-scale content from the wavefronts. This difference will appear as small-scale features in the differential OPD field. Another possible reason is the presence of the ghost beams overlapping with the main beam. Although we attempted to remove the effect of the ghost beams, as demonstrated in Fig. 7, other ghost beams might be too close to the main peak to be properly removed without affecting the main peak. In future work, we will modify the setup to eliminate the ghost beams.

As described previously, we also constructed the synthetic wavefront using complex fields from the green and red beams. A representative frame of the unwrapped synthetic wavefront is shown in Fig. 10(c), along with that of the red and green beams in Figs. 10(a) and 10(b). The wavefront of the synthetic beam indeed shows the same large-scale structure as the independently unwrapped red and green beams. Small-scale structures are less visible in the synthetic wavefront due to partial noise cancellation when combining the red and green beam complex fields, a well-known effect associated with the synthetic wavefront reconstruction.[17]

The computed $\mathrm{OPD}_{\mathrm{rms}}$ values, defined in Eq. (8), with associated error values, for the red beam, the green beam, and the synthetic wavelength are presented in Fig. 11. The error bars were calculated using a standard error analysis of time-resolved data.[22] $\mathrm{OPD}_{\mathrm{rms}}$ values match closely at each flow speed, further confirming the wavelength-independent performance of the

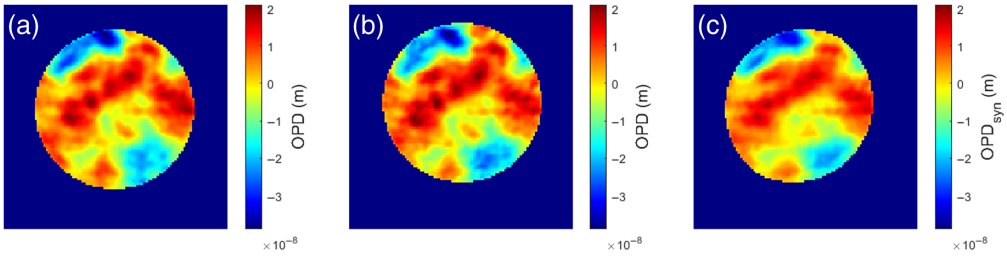


Fig. 10 Reconstructed OPD fields for the fully overlapping case. (a) OPD measured with the green (532 nm) beam. (b) OPD measured with the red (640 nm) beam after shifting by the pixel offset. (c) OPD of the synthetic wavelength.

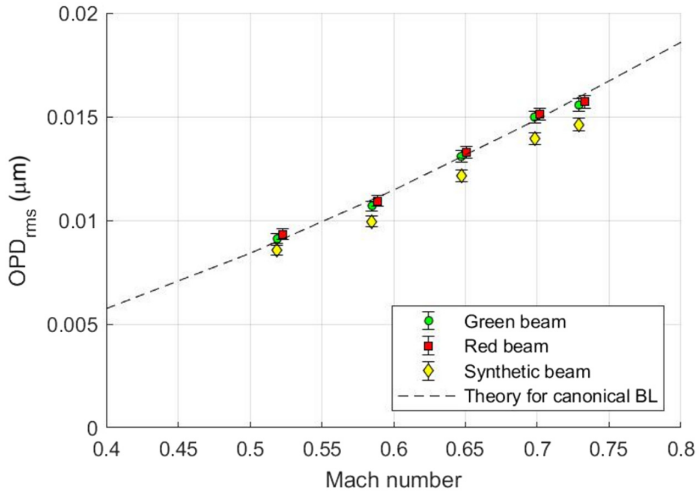


Fig. 11 OPD_{rms} and associated error bars for red, green, and synthetic beams as a function of the freestream Mach number and the comparison with the theoretical model for canonical boundary layers.[21] OPD_{rms} values for the red beam are slightly shifted in the horizontal direction for clarity.

dual-wavelength digital holography system. However, for each tested flow speed, the OPD_{rms} of the red beam is consistently slightly higher than that of the green beam. As discussed before, this bias is attributed to a slightly larger amount of small-scale features present in the red beam and/or residual ghost-beam presence in the Fourier plane that could not be entirely suppressed. The OPD_{rms} values of the synthetic wavefront are consistently lower than those of the red and green beams. This is likely caused by a partial noise cancellation between the green and red beams, as discussed above. Importantly, the measurements for the independently reconstructed red and green beams closely follow the overall optical distortions from the canonical boundary layer model[21] (dashed line), providing additional validation of the fully overlapped results.

4.2 Separated Beams Case

In the previous work,[23,24] SHWFS was used to collect and analyze wavefronts over two separate apertures using the same experimental facilities as in the present work. The purpose of that work was to investigate the convective nature of boundary layer wavefronts to test the limits of the frozen field assumption, a model of simple convection. It was found that for large aperture separations of three to four boundary layer thicknesses, a convective-only model of wavefront propagation was not sufficient to characterize the downstream wavefront from upstream data.

One of the goals of the presented work is to continue studying possible ways to predict the wavefronts over the downstream aperture using the wavefronts collected over the upstream aperture. Thus, similar experiments were conducted using a dual-beam DHWFS for two separations between the red and green beams of 40 mm (2δ) and 60 mm (3δ). The convective-only model assumes that the aero-optical structures simply convect with a constant convective speed. To compute the mean spatial correlation as a function of time and spatial separation, we performed a time-lagged cross-correlation between green and red beam OPD reconstructions for each of the

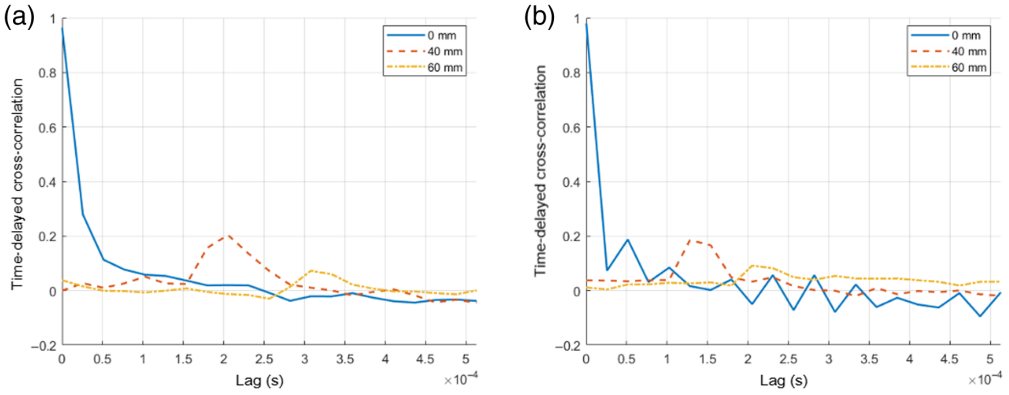


Fig. 12 Cross-correlation as a function of time delay for the freestream Mach number of (a) $M = 0.52$ and (b) $M = 0.73$.

three beam separations, including the fully overlapped case of 0 mm. For each pixel, the time series $\mathrm{OPD}_1(x, y, t)$ and $\mathrm{OPD}_2(x, y, t+\tau)$ are treated as vectors. For each pixel, the normalized time-delayed cross-correlation coefficient is given as

$$r_{xy}(\tau) = \frac{\sum_t \mathrm{OPD}_1(x, y, t)\mathrm{OPD}_2(x, y, t+\tau)}{\mu_{1,xy}\mu_{2,xy}}, \tag{10}$$

where $\mu_{1,xy}$ and $\mu_{2,xy}$ are the temporal standard deviations of $\mathrm{OPD}_1(x, y, t)$ and $\mathrm{OPD}_2(x, y, t+\tau)$, respectively, for that pixel. The resulting correlation coefficients were then averaged across all pixels valid in both frames to obtain the frame-wise correlation coefficient for each time lag. Figure 12 shows two such cross-correlation functions for all three spatial beam separations at the fastest and slowest flow speeds. In Fig. 12(a), the cross-correlation function is shown for the $M = 0.52$ case, and Fig. 12(b) shows that of the $M = 0.73$ data. The location of the peak represents the time delay required for the aero-optical structures to convect from the upstream aperture to the downstream aperture. The value of the peak is related to the degree to which the density fluctuations change spatially during the time they convect among the apertures. The normalized value of 1 means that the wavefronts are completely unchanged and simply convect among the apertures. The deviation of the value from 1 indicates the amount of warping of the density structures between the two apertures.

The x-values of the peaks are further apart in the $M = 0.52$ case than in the $M = 0.73$ case, as is expected for lower convective speeds. For the separation of 40 mm $= 2\delta$, the maximum value of the cross-correlation is ~0.2, and it drops further to 0.1 for the beam separation of 60 mm $= 3\delta$. This indicates that, for these large beam separations, the aero-optical structures changed very significantly among the apertures, which is consistent with similar observations.[23,24] Therefore, at spatial separations of $\approx 2\delta$, the convective-only model does not hold. These results are very similar across flow speeds, indicating that the rate of decorrelation is largely spatially dependent, not temporally.

To compute the convective speed of the density structures, we performed a two-dimensional Fourier-transform-based dispersion analysis on the upstream wavefront for each flow speed. In this analysis, we flattened each two-dimensional (2D) array at a given time step into a one-dimensional signal by selecting a small band of y-values at the center of the image and averaging across this y-value band for each pixel in the streamwise x-direction. After subtracting the time average at each x-location, a 2D Fourier transform was then computed, producing the spectral power density as a function of streamwise wavenumber and angular frequency. The slope of the diagonal band corresponding to the convective velocity was then extracted and used to compute the convective speed U_c. A table of convective velocities, U_c, computed using dispersion analysis and normalized by the corresponding freestream speeds, U_∞, measured by Pitot probe, is given in Table 2 for all measured Mach numbers.

The convective speed values, which vary from $0.79U_\infty$ to $0.83U_\infty$, match closely with the values predicted by previously studied relationships between freestream and convective speeds of the aero-optical distortions for the canonical subsonic boundary layers of $0.82U_\infty$,[21] providing

Table 2 Freestream Mach numbers and the ratio between convective and freestream velocities, for each flow speed.

M_∞	U_c/U_∞
0.52	0.83
0.59	0.82
0.65	0.79
0.70	0.78
0.73	0.79

strong evidence that the quantities measured in this experiment are physical structures rather than optical artifacts.

5 Conclusions

In this paper, we presented the design, implementation, and validation of a dual-wavelength/dual-beam digital holography wavefront sensor for quantitative imaging of boundary layer aero-optical distortions. The sensor reconstructs optical path difference fields from two laser beams of different wavelengths, enabling high-resolution measurements of density-induced wavefront distortions simultaneously at two spatial locations. To validate the sensor, we measured aero-optical distortions over both the fully overlapped and the separated beams at a range of subsonic Mach numbers in a subsonic compressible boundary layer flow at the Trisonic Wind Tunnel facility at Hessert Laboratory for Aerospace Research at the University of Notre Dame. Our comparative analysis of the fully overlapping beams demonstrated strong agreement among the OPD fields reconstructed from each wavelength, with differential errors largely independent of flow speed. The normalized root mean squared spatial error among the beams ranges from 17% to 21%, with the largest error corresponding to the smallest speed. These relatively small errors validate the method's ability to reconstruct the same optical field from independent beams. Possible sources contributing to the error were identified and discussed. Successful synthetic wavefront reconstruction was briefly demonstrated, indicating the ability of the sensor to function in the dual-wavelength configuration. Dispersion analysis techniques yielded convective speed estimates that matched closely with expected values across all Mach numbers. Although measurable error sources still exist when comparing reconstructed wavefronts and known flow properties, these errors are small, and the results demonstrate that dual-wavelength digital holography holds strong potential for high spatial resolution measurement of aero-optically aberrated wavefronts at different spatial regions of the flow. This technique is scalable to additional beams with different wavelengths, being constrained only by the ability to separate multiple beams in Fourier space and the increased noise associated with each additional beam.

Future work will focus on applying this approach to flows with stronger density gradients such as shocks, where the synthetic wavelength phase map associated with dual-wavelength digital holography is expected to significantly improve phase unwrapping and wavefront reconstruction compared with single-beam digital holography. The dual-beam configuration of the setup will also be used to study the ability to predict the wavefronts over the downstream aperture based on the wavefront information over the upstream aperture, which might provide an alternative approach to mitigate the latency problem in traditional closed-loop adaptive-optics systems.

Disclosures

The U.S. Government is authorized to reproduce and distribute reprints for governmental purposes notwithstanding any copyright notation thereon. The authors declare that they have no financial interests, commercial affiliations, or other potential conflicts of interest that could have influenced the objectivity of this research or the writing of this paper.

Distribution Statement A. Approved for public release: distribution is unlimited.

Code and Data Availability

Due to institutional restrictions, the data and code supporting this study are not publicly available. Summary results and additional methodological details are available from the authors upon reasonable request.

Acknowledgments

This work was sponsored by the Joint Directed Energy Transition Office. The authors would like to thank Zareb Noel for his help with the optical setup.

References

1. H. Barrell, J. Sears, and E. J., "The refraction and dispersion of air and dispersion of air for the visible spectrum," *Philos. Trans. R. Soc. Lond. Ser. A Math. Phys. Sci.* **238**(786), 1–64 (1939).
2. S. Gordeyev, E. J. Jumper, and M. Whiteley, *Aero-Optical Effects: Physics, Analysis and Mitigation*, Wiley Series in Pure and Applied Optics, Wiley (2023).
3. M. Kalensky et al., "Aero-optical effects, part II. Sources of aberrations: tutorial," *J. Opt. Soc. Am. A* **41**, 2175–2187 (2024).
4. M. Kalensky et al., "Aero-optical effects, part I. System-level considerations: tutorial," *J. Opt. Soc. Am. A* **41**, 2163–2174 (2024).
5. J. W. Goodman and R. W. Lawrence, "Digital image formation from electronically detected holograms," *Appl. Phys. Lett.* **11**, 77–79 (1967).
6. U. Schnars and W. Jüptner, "Direct recording of holograms by a CCD target and numerical reconstruction," *Appl. Opt.* **33**, 179–181 (1994).
7. E. Cuche, F. Bevilacqua, and C. Depeursinge, "Digital holography for quantitative phase-contrast imaging," *Opt. Lett.* **24**, 291–293 (1999).
8. U. Schnars and W. Jüptner, *Digital Holography: Digital Hologram Recording, Numerical Reconstruction, and Related Techniques*, Springer, Berlin/Heidelberg (2004).
9. C. C. Wilcox et al., "Digital holography wavefront sensing with a supersonic wind tunnel," *Proc. SPIE* **11030**, 110300L (2019).
10. M. T. Banet, M. F. Spencer, and R. A. Raynor, "Digital-holographic detection in the off-axis pupil plane recording geometry for deep-turbulence wavefront sensing," *Appl. Opt.* **57**, 465–475 (2018).
11. E. D. Chu, T. J. Bukowski, and S. Gordeyev, "Improved wavefront reconstruction for Shack–Hartmann wavefront sensor in the presence of shock-related distortions," *Opt. Laser Technol.* **187**, 112764 (2025).
12. M. F. Spencer, "Spatial heterodyne," in *Encyclopedia of Modern Optics*, second edition, B. D. Guenther and D. G. Steel, Eds., pp. 369–400, Elsevier, Oxford (2018).
13. M. A. Herráez et al., "Fast two-dimensional phase-unwrapping algorithm based on sorting by reliability following a noncontinuous path," *Appl. Opt.* **41**, 7437–7444 (2002).
14. R. Guo et al., "Robust and fast dual-wavelength phase unwrapping in quantitative phase imaging with region segmentation," *Opt. Commun.* **510**, 127965 (2022).
15. J. Gass, A. Dakoff, and M. K. Kim, "Phase imaging without 2π ambiguity by multiwavelength digital holography," *Opt. Lett.* **28**, 1141–1143 (2003).
16. J. Kühn et al., "Real-time dual-wavelength digital holographic microscopy with a single hologram acquisition," *Opt. Express* **15**, 7231–7242 (2007).
17. J. Di et al., "Improvement of measurement accuracy in digital holographic microscopy by using dual-wavelength technique," *J. Micro/Nanolithogr. MEMS MOEMS* **14**(4), 041313 (2015).
18. R. Guo and F. Wang, "Compact and stable real-time dual-wavelength digital holographic microscopy with a long-working distance objective," *Opt. Express* **25**, 24512–24520 (2017).
19. T. C. Khoo, A. Sharikova, and A. Khmaladze, "Dual wavelength digital holographic imaging of layered structures," *Opt. Commun.* **458**, 124793 (2020).
20. M. Huang, H. Qin, and Z. Jiang, "Real-time quantitative phase imaging by single-shot dual-wavelength off-axis digital holographic microscopy," *Appl. Opt.* **60**, 4418–4425 (2021).
21. S. Gordeyev et al., "Experimental studies of aero-optical properties of subsonic turbulent boundary layers," *J. Fluid Mech.* **740**, 214–253 (2014).
22. A. M. Law, Chapter 4 in *Simulation Modeling and Analysis*, 5th ed., McGraw-Hill Education, New York (2015).
23. M. R. Kemnetz, W. R. Burns, and S. Gordeyev, "Multiple aperture approach for the study of large-scale boundary-layer structures," in *47th AIAA Plasmadyn. Lasers Conf.*, AIAA Paper 2016-3530 (2016).
24. M. R. Kemnetz and S. Gordeyev, "Multiple aperture approach to wavefront prediction for adaptive-optic applications," in *55th AIAA Aerosp. Sci. Meeting*, AIAA Paper 2017-1344 (2017).

James Mitchell is a master's student in Aerospace and Mechanical Engineering at the University of Notre Dame, where he works in the Hessert Laboratory as part of the Aero-Optics Group under

the guidance of Professor Stanislav Gordeyev. His research focuses on off-axis digital holography for aero-optical wavefront sensing, including dual-wavelength and dual-beam techniques. His work combines optical system design with Fourier-based signal processing to characterize turbulent flows. He received his BS degree in physics from the University of Notre Dame.

Stanislav Gordeyev is an associate professor at the Department of Aerospace and Mechanical Engineering, University of Notre Dame, and a director of the Aero-Optics Group. His research interests include experimental investigation of aero-optical distortions caused by compressible turbulent flows at transonic, supersonic and hypersonic speeds. He is also actively involved in aero-optical and reduced-order modeling, wavefront sensor development, and flow control.